Optimal Cyclic Control of an Ocean Kite System in a Spatiotemporally Varying Flow Environment

James Reed[1], Joshua Daniels[2], Ayaz Siddiqui[3], Mitchell Cobb[4], Michael Muglia [5] and Chris Vermillion [6]

***Abstract*— This paper presents a technique for maximizing the power production of a tethered marine energy-harvesting kite performing cross-current figure-eight flight in a 3D spatiotemporally varying flow environment. To generate a net positive power output, the kite employs a cyclic spooling method, where the kite is spooled out while flying in high-tension cross-current figure-eight flight, then spooled in radially towards the base-station under low tension. The present work focuses on two key contributions. First, we present a transition controller for robustly switching between power-generating cross-current spool-out operation and low-tension (power-consuming) spool-in operation under variable flow conditions. Second, we present an optimization that selects spool-out speeds and mean elevation angles for the kite during the spool-out phase such that the net power produced per spooling cycle is maximized. Simulation results for a six-degree-of-freedom kite model in a 3D spatiotemporally varying flow environment (which superimposes high-frequency turbulence onto a low-frequency flow field) are shown for a baseline case as well as an optimized case. These simulation results show robust transition, along with a 9.3 percent cycle-averaged power output increase as a result of the optimization.**

I. Introduction

Marine hydrokinetic (MHK) energy-harvesting systems are growing in popularity for creating power at both the utility scale and the consumer scale. The potential application areas for these devices include both ocean and riverine environments. In the ocean, there is estimated to be 334 TWh/year of usable tidal energy [1] and 163 TWh/year of usable ocean current energy [2] in the waters surrounding the coastal areas of the United States. To utilize these resources, hydrokinetic energy-harvesting systems are being developed for both grid connection and for powering microgrids [3]. The summation of the resources in the waters surrounding the coastal United States is large enough to power millions of homes at a utility-scale as well as research buoys, navigational aids, autonomous underwater vehicles, and other devices that comprise what is termed the "blue economy" [4]. One of the challenges with harvesting these resources is that the areas with the most significant resources are typically found at tremendous depths. For example, the region of the Gulf Stream with the highest energy density is often found in areas that exceed 1 km of depth [5].

The challenge of harvesting ocean energy resources in deep waters bears resemblance to the challenge of high-altitude wind energy harvesting, where the winds at 500-1000 meter altitudes often have the peak power densities [6]. In the wind energy community, a solution has been developed, in the form of tethered airborne energy-harvesting "kites" (which can take the form of either fabric kites or rigid wings), capable of being deployed at high altitudes to reach the areas with higher power densities without incurring significant structural costs associated with building towered turbines capable of reaching similar altitudes. Example systems have been developed by [7], [8], [9], and [10]. Using many of the important advancements in the airborne kite energy field, underwater energy-harvesting kites are being developed in both industry [11] and academia (see [12], [13], and [14]), to cost-effectively reach areas possessing swifter currents. Furthermore, by executing rapid cross-current motions perpendicular to the prevailing current flow, energy-harvesting kites can fly at speeds 5-10 times greater than the prevailing current speed, ultimately delivering more than an order of magnitude more power per unit mass than their towered counterparts [15]. This makes kite-based systems a cost-effective solution in lower-flow areas where fixed turbines are not cost effective.

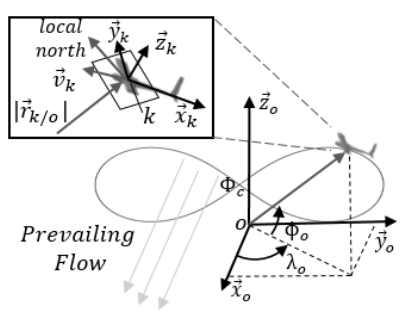

Fig. 1. Concept of operations for a marine energy-harvesting kite undergoing cyclic figure-eight motions. The above figure also shows the k and o frame orthonormal coordinate systems, spherical angles ϕ_o and λ_o, as well as the path center elevation angle Φ_c.

Energy-harvesting kites can create power from the prevailing flow either through on-board turbines or cyclic spooling motion using a winch/generator combination. This work

This research was supported by the Department of Energy, award number DE-EE0008635.

[1]James Reed is a graduate student at North Carolina State University jcreed2@ncsu.edu.

[2]Joshua Daniels holds a Bachelor's degree in Aerospace Engineering from North Carolina State University. jldanie5@ncsu.edu.

[3]Ayaz Siddiqui is a PhD candidate at North Carolina State University asiddiq2@ncsu.edu.

[4]Dr. Mitchell Cobb is a PhD recipient from North Carolina State University and Controls Engineer at Blue Origin mcobb@ncsu.edu.

[4]Dr. Michael Muglia is a Research Assistant Professor at the Coastal Studies institute, Wanchese, NC 27981 muglia@ecu.edu.

[6]Dr. Chris Vermillion is an Associate Professor in the Department of Mechanical and Aerospace Engineering at North Carolina State University, Raleigh, NC 27695, USA cvermil@ncsu.edu. He is also a technical advisor and equity stakeholder for Altaeros Energies, Inc. and Windlift, LLC

focuses on the spooling method of energy generation, where the kite is cyclically spooled out under high tension, in cross-current motions, then spooled in under low tension, thereby generating net positive energy output over each cycle. Optimization of many different elements of kite control have been explored. Loyd's seminal work [15] provides upper bounds on the power that can be generated through cross-current kite motion and identifies the optimal kite spool-out speed to be one-third of the prevailing flow speed. However, this is based on a 2D quasi-static analysis, which does not consider the implications of the kite's dynamics and closed-loop control. Work in [16] has explored optimal crosswind flight trajectories, work in [17] has explored optimal roll angle control for airborne kites, and [18] has optimized cross-current trajectories for an underwater kite. Furthermore, previous work by the co-authors, including [19] and [20] has addressed cyclic control aspects of the kite control problem, using iterative learning techniques to adapt the path in [19] and Pontryagin's maximum principle to derive optimal spooling strategies in [20]. Furthermore, [20] focuses on a restrictive spooling strategy where the net spooling over a single figure-8 cycle is zero. As an initial effort in accounting for the spatial variability of the resource, [21] investigates the optimal elevation angle regions for an airborne kite, based on kite dynamics and an assumed wind shear profile. While the aforementioned papers address challenges associated with the optimization of kite flight trajectories, their optimizations do not account for the spatiotemporally varying flow field, nor is this flow field accounted for in the presented results.

Demonstration of robust operation and optimization of power output in a realistic spatiotemporally varying flow field remains an important research topic that is addressed in the present paper. In particular, our work focuses on three key elements, which advance the field through the cyclic control of an ocean kite system in a realistic spatiotemporally varying flow field:

1) We describe a transition controller for an underwater kite, which robustly allows the kite to fly in cross-current motions while spooling out, then transition to flying radially in towards the base-station while spooling in, and vice-versa.
2) We present an optimization algorithm for maximizing power production in a spatiotemporally varying flow field by optimizing the kite's spool-out rate and path center elevation angle.
3) We show simulation results for a six-degree-of-freedom kite model operating in a spatiotemporally varying environment, which is based on the superposition of a high-frequency turbulence model on top of a Mid-Atlantic Bight South Atlantic Bight Regional Ocean Model (termed the "MSR Model" in this work). Using this simulation environment, we compare the optimized case to a baseline case demonstrating an increase in cycle averaged power output.

II. Plant Model

Following our earlier work in [22], the MHK kite is modeled as a combination of a rigid lifting body wherein forces and moments are calculated from lift, drag, buoyancy, and gravity, and a lumped mass tether model whose links are characterized as non-compressive spring-damper elements, as in [23]. The dynamics of the kite in this paper are formulated using the method prescribed by [24] to allow for the inclusion of added mass terms. The instantaneous power produced by the system $P_{gen}(t)$, is modeled as:

$$P_{gen}(t) = ||\vec{F}_{Thr}||v_{sp}, \tag{1}$$

where v_{sp} is the spool speed of the tether, and $\vec{F}_{Thr}$ is the force from the kite's tether.

As indicated in Fig. 1, the coordinate system used for the kite is described by three body-fixed orthonormal unit vectors, $\vec{x}_k$, $\vec{y}_k$, and $\vec{z}_k$, whose origin lies at the kite's center of mass. An additional ground-frame coordinate system is described by orthonormal unit vectors $\vec{x}_o$, $\vec{y}_o$, and $\vec{z}_o$, also indicated in Fig. 1. The state variables describing the position and orientation (and rates of change of the position and orientation) of the kite evolve according to the nonlinear equations of motion:

$$\dot{\mathbf{v}} = \mathrm{M_k}^{-1}\left(\tau(\mathbf{v}_r) - \mathbf{C}\left(\mathbf{v}_r\right)\mathbf{v}_r\right), \tag{2}$$

where

$$\mathbf{v}_r = \begin{bmatrix} u_{\text{kite}} - u_f \\ v_{\text{kite}} - v_f \\ w_{\text{kite}} - w_f \\ p \\ q \\ r \end{bmatrix}. \tag{3}$$

The variables u_{kite}, v_{kite}, and w_{kite} are the components of the kite's velocity aligned with the axes of k frame, and u_f, v_f, and w_f are the components of the flow velocity aligned with the k frame. Additionally, p, q, and r are the rotational rates about the kite's body axes. The collection of roll (ϕ_k), pitch (θ_k), and yaw (ψ_k) Euler angles describing this system are given by $\vec{\mu_k} \triangleq [\ \phi_k \quad \theta_k \quad \psi_k\ ]^T$.

The vector τ is comprised of the external forces and moments and is given by

$$\tau = \begin{bmatrix} \vec{F}_{Net} \\ \vec{M}_{Net} \end{bmatrix} \tag{4}$$

where $\vec{F}_{Net} \in \mathbb{R}^3$ is the vector containing the external forces on the kite, and $\vec{M}_{Net} \in \mathbb{R}^3$ is the vector containing the external moments on the kite. These include fluid dynamic forces and moments, which depend on $\mathbf{v}_r$, gravitational/buoyant forces (and associated moments), and the external force (and associated moment) from the tether. Additionally, $\mathbf{C}\left(\mathbf{v}_r\right) \in \mathbb{R}^{6\times 6}$ is the matrix accounting for the Coriolis and centripetal terms arising from rigid body and added mass effects.

Finally, the matrix $\mathrm{M_k} \in \mathbb{R}^{6\times 6}$ is the mass matrix of the kite, which is a combination of mass and inertia terms, coupling terms due to the body frame origin not being at

the kite's center of mass, and added mass terms calculated based on the kite's geometry. Readers are referred to [24] for further details regarding the calculation of the matrices $\mathrm{M_k}$ and $\mathbf{C}(\mathbf{v}_r)$.

The kite is subjected to forces and moments arising from five surfaces (a fuselage, port wing, starboard wing, horizontal stabilizer and vertical stabilizer), buoyancy, gravity, and the tether. These forces and moments are calculated as:

$$\begin{aligned}\vec{F}_{Net} =& \vec{F}_{Line,1} + (V\rho - m)\, g\vec{z}_o \\ &+ \frac{1}{2}\rho A_r \sum_{i=1}^{5} \|\vec{v}_{a_i}\|^2 \left(C_{L,i}\vec{u}_{L,i} + C_{D,i}\vec{u}_{D,i}\right)\end{aligned} \tag{5}$$

$$\vec{M}_{Net} = \frac{1}{2}\rho A_r \sum_{i=1}^{5} \|\vec{v}_{a_i}\|^2 \vec{r}_{a_i} \times \left(C_{L,i}\vec{u}_{L,i} + C_{D,i}\vec{u}_{D,i}\right) \tag{6}$$

where in (5), the first term is the force exerted at the center of mass (CM) of the kite by the tether on the lifting body, the second term describes the net buoyant force, and the last term describes the fluid dynamic forces. Here, V is the volume of the kite, ρ is the fluid density, m is the mass of the system, and g is the acceleration due to gravity. The net moment applied to the system, $\vec{M}_{Net}$, is then calculated as the sum of the cross products of the individual fluid dynamic forces, as described by the last term in (5), and the appropriate associated moment arm, r_{a_i}:

$$\vec{M}_{Net} = \frac{1}{2}\rho A_r \sum_{i=1}^{5} \|\vec{v}_{a_i}\|^2 \left(C_{L,i}\vec{u}_{L,i} + C_{D,i}\vec{u}_{D,i}\right) \times \vec{r}_{a_i}. \tag{7}$$

The index, i, refers to each of the five aforementioned surfaces. The force on each surface depends on the apparent flow at the hydrodynamic center of that particular surface, which is calculated as:

$$\vec{v}_{a_i} = \vec{v}_f(t, \vec{r}_{k/o} + \vec{r}_{a_i}) - (\vec{v}_k + \omega \times \vec{r}_{a_i}), \tag{8}$$

where $\vec{v}_f(\cdot, t)$ is the spatially-varying flow profile, $\vec{v}_k$ is the kite's velocity, and $\vec{r}_{a_i}$ is the vector from the CM of the kite to the fluid dynamic center of the ith surface. The fluid dynamic coefficients of (5) and (7) are obtained by modeling each fluid dynamic surface independently in the Athena Vortex Lattice (AVL) software created by [25] and parameterizing them as functions of the associated control surface deflections, δ_i, as:

$$\begin{aligned}C_{(L,D),i}(\vec{v}_{a_i}) &= C_{(L_0,D_0),i}(\vec{v}_{a_i}) + C_{(L_1,D_1),i}\delta_i \\ &\quad + C_{(L_2,D_2),i}\delta_i^2\end{aligned} \tag{9}$$

where the control sensitivity coefficients, $C_{L_1,i}$, $C_{L_2,i}$, $C_{D_1,i}$, and $C_{D_2,i}$ are obtained from AVL. The spanwise lift coefficient distributions, $C_{l,i}(y)$, obtained from the software are heuristically corrected to account for nonlinear stall behavior that is not present in AVL.

Finally, the kite's tether is modeled as a chain of non-compressive spring-dampers (links), connected with point masses (nodes), subjected to buoyancy, gravity, and drag. The total force at the kite from the kite's tether, which acts at the kite's center of mass, denoted by the point k, is ultimately calculated by the tether model and is given by $\vec{F}_{Thr}$. Readers are referred to [26] for a detailed description of the tether model.

III. Spatiotemporally Varying Flow Field Model

The flow field, which is characterized as a function of depth ($\vec{z}_o$), down-current location, ($\vec{x}_o$), cross-current location ($\vec{y}_o$), and time (t), is computed as the superposition of a low-frequency flow profile and high-frequency turbulence model as follows:

$$\tilde{V}_{comb}(\vec{x_o}, \vec{y_o}, \vec{z_o}, t) = \tilde{V}_{turb}(\vec{x_o}, \vec{y_o}, \vec{z_o}, t) + \tilde{V}(\vec{z_o}, t), \tag{10}$$

where $\tilde{V}(\vec{z_o}, t)$, $\tilde{V}_{turb}(\vec{x_o}, \vec{y_o}, \vec{z_o}, t)$, and $\tilde{V}_{comb}(\vec{x_o}, \vec{y_o}, \vec{z_o}, t)$ represent the low-frequency flow field, high-frequency turbulent field, and combined flow model, respectively. Because the total cross-current motion of the kite spans a tiny fraction of the total current resource (e.g., the Gulf Stream), spatial variations in $\vec{y_o}$ and $\vec{x_o}$ are neglected in the low-frequency model.

The low frequency model used in this work is the Mid-Atlantic Bight South-Atlantic Bight Regional Ocean Model (MSR). This model, which was developed by North Carolina State University's Ocean Observing and Modeling Group, provides current profiles at 42 different locations in the Gulf Stream at 25 m vertical resolution. The MSR model is detailed in [27].

The turbulent high-frequency components of the ocean currents are calculated based on a discretization of the flow velocity's power spectral density (PSD) equation. Specifically, the model leverages fundamental techniques described in [28] to generate a spatiotemporally varying turbulence profile that can be applied to the hydrodynamic center of each component in the dynamic model. Based on inputs of turbulence intensity, time-averaged flow velocity profile, a specified frequency range, standard deviations, and spatial correlation coefficients for the flow velocities, the model outputs a spatial grid of time-varying velocity vectors.

IV. Control Details

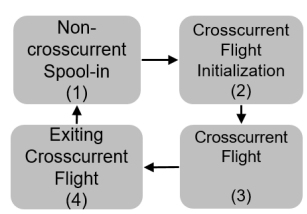

Fig. 2. Multi-cycle spooling controller state machine.

The kite's control system consists of a lower-level "base" hierarchical flight control structure, along with an upper-level state machine, shown in Fig. 2 that modifies features of the lower-level controller based on whether the kite is in power-generating cross-current spool-out motion, power-consuming spool-in motion, or transitioning. While the structure of the lower-level controller remains consistent, the calculations change based on the mode that the system is in. Furthermore, certain levels of the hierarchical controller are deactivated

within certain modes of the state machine (for example, the level of the hierarchical controller that computes a target velocity vector to track a prescribed figure-8 flight path is only active during the cross-current flight mode). The flight controller is accompanied by a spooling controller, which optimizes the spool-out speed profile and elevation angle profile prior to each cycle, based on the flow velocity data acquired during the previous cycle.

A. Lower Level Flight Controller

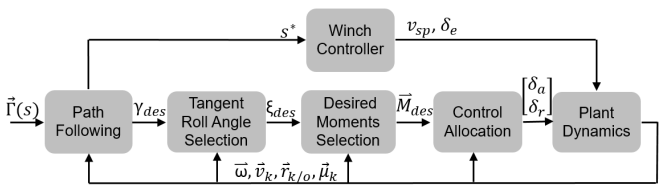

Fig. 3. Hierarchical flight controller.

The lower-level flight controller assumes a hierarchical structure (shown in Fig. 3), consisting of four levels: (i) selection of a target velocity angle, (ii) selection of a target tangent roll angle, (iii) selection of a target moment vector, and (iv) a control allocation module that computes control surface deflections to achieve the target moment vector.

1) Target Velocity Angle Calculation: The target cross-current path, $\vec{\Gamma}(s)$, is specified in Cartesian coordinates based on the Lemniscate of Booth, defined by a_{booth} and b_{booth} in [29]. This path is constrained to lie on the surface of a sphere centered at the point o, as shown in Figure. 1. The variable s is defined as a path parameter that varies from 0 to 2π. Given this path, the controller calculates a three-dimensional vector representing the desired direction of the kite's velocity vector, which is computed as a weighted average between the *perpendicular vector*, $\vec{p}_\perp^*$, and the *parallel vector*, $\vec{p}_\parallel^*$. The perpendicular vector is given by:

$$\vec{p}_\perp^* = \frac{\hat{p}_\perp}{\|\hat{p}_\perp\|} \quad \text{where} \quad \hat{p}_\perp = \begin{bmatrix} (\vec{\Gamma}(s^*) - \vec{x}) \cdot \vec{u}_{\Phi_o}(\vec{x}) \\ (\vec{\Gamma}(s^*) - \vec{x}) \cdot \vec{u}_{\lambda_o}(\vec{x}) \\ 0 \end{bmatrix}. \quad (11)$$

Here, $\vec{u}_{\Phi_o}(\vec{x})$ and $\vec{u}_{\lambda_o}(\vec{x})$ are unit vectors in the elevation (Φ_o) and azimuth (λ_o) directions shown in Fig. 1, sometimes referred to as "local north" and "local east." The parallel vector, $\vec{p}_\parallel^*$, is a unit vector that lies parallel to the path at the path variable corresponding to the closest point on the path, s^*, and is calculated by:

$$\vec{p}_\parallel^* = \frac{\hat{p}_\parallel}{\|\hat{p}_\parallel\|} \quad \text{where} \quad \hat{p}_\parallel = \left.\frac{d\vec{\Gamma}}{ds}\right|_{s=s^*}. \quad (12)$$

In (11) and (12), the closest point on the path is described by the path variable s^*, which is the solution to the minimization problem:

$$s^* = \arg\min_s \ \alpha(s), \quad \text{where}$$
$$\tan(\alpha(s)) = \frac{\|\vec{r}_{k/o} \times \vec{\Gamma}(s)\|}{\vec{r}_{k/o} \cdot \vec{\Gamma}(s)}. \quad (13)$$

Here, $\alpha(s)$ is the angle between the position vector, $\vec{r}_{k/o}$, and the path, $\vec{\Gamma}(s)$.

The desired velocity unit vector, $\vec{v}_{des}$, is then calculated as the linearly weighted sum of $\vec{p}_\perp^*$ and $\vec{p}_\parallel^*$, according to:

$$\overline{\alpha}(s^*) = \min\left\{\alpha(s^*), \alpha_0\right\}$$
$$\vec{v}_{des} = \left(1 - \frac{\overline{\alpha}(s^*)}{\alpha_0}\right)\vec{p}_\parallel^* + \frac{\overline{\alpha}(s^*)}{\alpha_0}\vec{p}_\perp^*. \quad (14)$$

Here, α_0 serves as an upper limit on the angle used in the weighting.

The velocity angle, γ, which describes the orientation of a given velocity vector on the sphere of radius $\|\vec{r}_{k/o}\|$ at the current position $\vec{r}_k/o$, is given by

$$\gamma(\vec{v_k}) = \arctan\left(\frac{\vec{v_k} \cdot \vec{u}_{\Phi_o}(\vec{r}_{k/o})}{\vec{v_k} \cdot \vec{u}_{\lambda_o}(\vec{r}_{k/o})}\right). \quad (15)$$

The desired velocity angle is therefore given by $\gamma(\vec{v}_{des})$.

2) Tangent Roll Angle Controller: The next level of the flight controller maps $\gamma(\vec{v}_{des})$ to a desired tangent roll angle, ξ_{des}, where ξ describes the kite's orientation relative to the tangent plane and is calculated as:

$$\tan(\xi(\vec{y}_k(t))) = \frac{\vec{y}_k \cdot (\vec{u}_{\lambda_o} \times \vec{u}_{\Phi_o})}{\sqrt{(\vec{y}_k \cdot \vec{u}_{\Phi_o})^2 + (\vec{y}_k \cdot \vec{u}_{\lambda_o})^2}}. \quad (16)$$

The desired tangent roll angle, ξ_{des}, is calculated using saturated proportional control, specifically:

$$\xi_{des} = \min\{\max\{k_\gamma(\gamma(\vec{v}) - \gamma(\vec{v}_{des})), \xi_{min}\}, \xi_{max}\}, \quad (17)$$

where k_γ is the proportional gain. Ultimately, adjustment of ξ re-vectors the kite's lift to provide the necessary force to re-align the kite's velocity angle with the target value and ultimately get the kite back on its target path.

3) Desired Moment Vector Controller: In selecting the desired moments, we set a target rolling moment to drive the tangent roll angle (ξ) to its setpoint (ξ_{des}), while simultaneously setting a target yaw moment to drive the side-slip angle, β, to zero. The combined elevator and tether spooling controller articulates the elevator to trim the system to a high angle of attack during spool-out and a low angle of attack during spool-in (which is described in the subsequent subsection). The desired moment vector set within the flight controller is given by:

$$\vec{M}_{des} = \begin{bmatrix} k_{p_L} e_\xi(t) + k_{i_L}\int_0^t e_\xi(t)d\tau + k_{d_L}\dot{e}_\xi(t) \\ 0 \\ k_{p_N}\beta + k_{i_N}\int_0^t \beta d\tau + k_{d_N}\dot{\beta} \end{bmatrix},$$

where $e_\xi(t) = \xi(\vec{y}_k(t)) - \xi_{des}$, and β is the fluid dynamic side-slip angle.

4) Control Allocation Module: In order to map the desired moment vector to control surface deflections, we invert a linearized approximation of the nonlinear mapping from deflections to hydrodynamic moments. This approximation is calculated by neglecting the effect of angular velocity on the apparent flow at each fluid dynamic surface, then linearizing to obtain an expression in the following form:

$$\vec{M}_{Net} = \vec{M}_o + A\vec{\delta}, \quad (18)$$

where $\vec{\delta} \triangleq [\ \delta_a\ \delta_e\ \delta_r]^T$ represents the deflection angles of the ailerons, elevator, and rudder, respectively. The variable $\vec{M}_o$ represents the moment vector that occurs with zero control surface deflections, and A is the matrix of linear control sensitivity coefficients. This results in a system of three equations and three unknowns, which are solved in computing the control surface deflections at each time instant.

B. Transition Controller

Our previous work focusing on optimal spool-out/spool-in control in [20] focused on an *intra-cycle* spooling strategy, where tether was spooled out and in within the same cross-current cycle, and cross-current flight was maintained throughout. While this strategy allows the kite to target areas of higher flow in the water column and does not require any transition into and out of cross-current motion, the lack of transition means that the kite expends more energy under spool-in operation than it would if it had transitioned out of cross-current motion for this phase of operation. In contrast, in a *multi-cycle* spooling technique, the kite spools out in figure-eight flight over multiple laps, and spools in radially towards towards the base-station in non-cross-current flight. To implement the multi-cycle spooling method, a transition controller using a state-machine has been developed. This controller has the following four modes of operation:

1) *non-cross-current spool-in*, where the kite is commanded to be maneuvered such that it has a roll Euler angle of zero, and is spooled in radially towards the base-station;
2) *crosscurrent flight initialization*, where the kite's spooling speed is set to zero and its elevator deflection is adjusted in order to increase its elevation angle, resulting in the necessary forward "launch" velocity to initiate cross-current flight;
3) *crosscurrent flight*, where the kite gains velocity by approaching the path from a high elevation angle, and once the path is reached, generates power by spooling out while flying perpendicular to the flow in figure-eight motions;
4) *exiting crosscurrent flight*, where the kite exits the figure-eight path and achieves a low angle of attack to prepare for the non-crosscurrent spool-in phase.

The state machine is displayed in Fig. 2, and the conditions for entering and exiting each mode of operation are shown in the Table I. In the following subsections, each mode of operation is shown in more detail.

1) Non-cross-current spool-in: In this mode of operation, the kite is radially spooled in towards the base station to a target elevation angle. With respect to the general hierarchical control structure, the velocity angle controller and tangent roll angle controller are deactivated, and the moment vector controller computes a moment that keeps the kite at a target Euler roll angle. Specifically, in order to stabilize lateral motion, the wings of the kite are kept level (at a roll Euler angle of zero). This is achieved by passing the difference between the roll angle and a setpoint of zero through a PID controller, giving a desired moment of the form

TABLE I

The table below describes the transition conditions between operation modes, where the mode numbers correspond to the numbering in Fig. 2.

Operation Mode	Transition Condition
1-2	$\|v_k\| < \|v_f\| K_{sg}$
2-3	$\|v_k\| > \|v_f\|$
3-4	$\|\vec{r}_{k/o}\| > r_{max}$ $\wedge\ (s^* > .25 \wedge s^* < .4)$ $\vee \|\vec{r}_{k/o}\| > r_{max}$ $\wedge\ (s^* > .75 \wedge s^* < .9)$
4-1	$\|v_k\| < \|v_f\|$

$$\vec{M}_{des} = \begin{bmatrix} -k_{p_L}\phi_k(t) + k_{i_L}\int_0^t -\phi_k(t)d\tau - k_{d_L}\dot{\phi}_k(t) \\ 0 \\ 0 \end{bmatrix}, \tag{19}$$

which is then implemented by the control allocation module (of the same form as Section IV-A.4). The control allocation module then ultimately controls the aileron and rudder deflections.

The elevator command is determined by

$$\vec{\delta}_e = \begin{cases} \delta_{e,max} & \vec{r}_{k/o}\vec{z}_o > z_{thr} \\ \min\{\max\{\left(1 - \dfrac{z_{thr} - \vec{r}_{k/o}\vec{z}_o}{z_{thr}}\right)\delta_{e,max} + \\ \left(\dfrac{z_{thr} - \vec{r}_{k/o}\vec{z}_o}{z_{thr}}\right)\delta_{e,min}, \delta_{e,max}\}, \delta_{e,min}\} & \text{otherwise,} \end{cases} \tag{20}$$

where $\delta_{e,max}$ is the maximum allowable elevator deflection, $\delta_{e,min}$ is the minimum allowable elevator deflection, and z_{thr} is the vertical threshold for which to begin the saturated weighted average between the maximum elevator deflection and minimum elevator deflection.

The commanded spool-in speed, v_{in}, is calculated as 1.5 times the magnitude of the flow speed:

$$v_{in} = -1.5\|\vec{v}_f\|. \tag{21}$$

2) Cross-current flight initialization: In this mode of operation, the first three levels of the hierarchical flight controller are deactivated, and the kite is released from the controlled equilibrium created during non-cross-current spool-in motion. Specifically, the spool-out speed is set to zero:

$$v_{sp} = 0, \tag{22}$$

and the elevator is deflected to a "launch angle" that corresponds to a greater equilibrium elevation angle, thereby accelerating the kite upward and producing the necessary velocity to initiate cross-current motion:

$$\vec{\delta} = \begin{bmatrix} 0 \\ \delta_{\text{e,launch}} \\ 0 \end{bmatrix}. \tag{23}$$

In performing this operation, the kite builds up speed as it moves from the forced low elevation angle towards a higher elevation angle. This mode is exited during this transient

motion, once the kite builds sufficient speed, as indicated in the transition conditions of Table I.

3) Cross-current flight: In this mode of operation, the kite follows a figure-eight path that perpendicular to the prevailing flow, with all four levels of the flight controller detailed in Section IV-A active. As described in detail in Section IV-A, the figure-8 flight path is described by the Lemniscate of Booth. The spool-out rate is commanded by a higher-level controller, detailed in Section IV-C.

4) Exiting cross-current flight: In this mode of operation, the kite exits the figure-eight path and prepares to be spooled in. This is achieved by commanding a desired moment vector of zero,

$$\vec{M}_{des} = \begin{bmatrix} 0 \\ 0 \\ 0 \end{bmatrix}, \tag{24}$$

to the control allocation module (of the same form as Section IV-A.4), which commands deflections for the kite's aileron and rudder.

The elevator is deflected to its maximum value, $\delta_{e,max}$, which causes the kite to assume a low angle of attack, in order to reduce tether tension for the spool-in phase. The resulting control surface deflection vector is then given by

$$\vec{\delta} = \begin{bmatrix} \delta_a \\ \delta_{e,max} \\ \delta_r \end{bmatrix}, \tag{25}$$

where δ_a and δ_r are commanded by the control allocation module.

C. Path Elevation Angle and Spool-Out Speed Optimization: Mathematical Formulation

The instantaneous mechanical power produced by the kite is given by

$$P_k = v_{sp} T_A, \tag{26}$$

where T_A is the available tension resulting from the flow and spool speed combination and v_{sp} is the spooling speed.

For a given angle of attack and side slip angle (as regulated by the closed-loop flight controller), the tether tension is proportional to the the apparent flow velocity squared:

$$T_A \propto \left((v_f - v_{sp} \cos(\Phi_c)) \cos(\Phi_c) \right)^2, \tag{27}$$

where Φ_c is the path center elevation angle, which is also the mean elevation angle of the kite for each lap of figure-eight flight. The form of the above equation arises from the fact that the kite is spooled at an angle above the horizontal. In this work, the largest component of the spatiotemporally varying flow velocity field is directed along the x_o axis, and so for this optimization, the flow field is approximated as a column of velocity vectors aligned with the x_o axis. In the ocean, the flow velocities tend to decrease with depth (due to the shear profile), which results in a trade-off in optimizing the Φ_c profile; lower values of Φ_c result in higher power output for a given flow speed, but larger values of Φ_c allow for operation at shallower depths, resulting in higher available flow speeds.

Given the expressions in equations (27) and (26), the kite's optimal spooling speed profile and path center elevation angle can be optimized through the following formulation:

$$\begin{aligned} \text{Maximize} \quad J_{cycle} = \frac{1}{t_{tot}} \int_{t_{o,i}}^{t_{o,f}} v_{out} * \\ \left((v_f - v_{out} \cos(\Phi_c)) \cos(\Phi_c) \right)^2 d\tau \end{aligned} \tag{28}$$

$$\text{Subject to:} \quad v_{out} \leq v_f,$$

where t_{tot} is the total spooling cycle time, $t_{o,i}$ is the starting time of the spool-out phase, and $t_{o,f}$ is the ending time of the spool-out phase. The spool-in speed is constant in this work and is given by equation (21).

D. Path Elevation Angle and Spool-Out Speed Optimization: Implementation

To reduce the elevation angle and spool-out speed profile optimization formulation to a finite-dimensional problem, the objective function in (28) was discretized and re-written as a function of discretized tether length during the spool-out phase. This results in a discretized objective function given by

$$\begin{aligned} J_{cycle} = \frac{1}{t_{tot}} \sum_{i_T=1}^{N_T} v_{out,i_T} \left((v_{f,i_T} - v_{out,i_T} \cos(\Phi_{c,i_T})) * \right. \\ \left. \cos(\Phi_{c,i_T})^2 (t_{i_T+1} - t_{i_T}). \right. \end{aligned} \tag{29}$$

Furthermore, if the tether length discretizations are equal, the following simplification can be made:

$$v_{out,i_T} = \frac{\frac{l_T}{N_T}}{(t_{i_T+1} - t_{i_T})}. \tag{30}$$

Equation (29) can then be re-written as

$$J_{cycle} = \frac{1}{t_{tot}} \sum_{i_T=1}^{N_T} \left((v_{f,i_T} - v_{out,i_T} \cos(\Phi_{c,i_T})) \cos(\Phi_{c,i_T}) \right)^2. \tag{31}$$

Additionally, the cycle time, t_{tot}, is calculated by

$$t_{tot} = t_{in} + \sum_{i_T=1}^{N_T} \frac{\frac{l_T}{N_T}}{v_{out,i_T}} \tag{32}$$

where t_{in} is a constant. The objective function shown in equation (31) is now entirely in terms of the decision variables, shown in matrix form as $\bar{\Phi}_c$ and $\bar{v}_{out}$, and the flow velocity at each tether length discretization. The matrices $\bar{\Phi}_c$ and $\bar{v}_{out}$ are defined as

$$\bar{\Phi}_c = \begin{bmatrix} \Phi_{c,1_T} \\ \vdots \\ \Phi_{c,N_T} \end{bmatrix} \text{ and } \bar{v}_{out} = \begin{bmatrix} v_{out,1_T} \\ \vdots \\ v_{out,N_T} \end{bmatrix}. \tag{33}$$

The objective function in equation (31) can be minimized using a non-linear optimization technique such as sequential quadratic programming, which was used in this work through the MATLAB optimization toolbox.

During the kite's operation, this optimization is performed during the fourth mode of operation, to compute $\bar{\Phi}_c$ and $\bar{v}_{out}$ for the next spool-out cycle. Available flow data from the previous cycle is used in performing the optimization. This serves as an accurate approximation for the flow speed as a function of depth for the next cycle, due to the time-scale separation between the time required to complete a cycle (hundreds of seconds) and the time scales associated with low-frequency flow variations (hours).

V. Results

In this section, we present results that compare the power production of the kite operating in a realistic turbulent ocean model under two different scenarios. The first scenario (baseline case) corresponds to a constant path center elevation angle of 20.6 deg. along with a constant spool-out speed of one-third of the current flow speed at the kite's center of mass, as prescribed by work in [15]. The second scenario corresponds to optimized path center elevation angle and spooling speed profiles, as prescribed by the higher-level controller optimization described in Section IV-C. The turbulent flow profile that the kite experiences varies as a function of time and spacial position, according to the aforementioned high-frequency turbulence model. Key parameters for the simulations are given in Table II.

TABLE II

Parameters used in simulation.

Variable	Description	Value	Units
A_r	Kite reference area	10	m^2
m_k	Kite mass	2830	kg
–	Kite span	10	m
a_{booth}	Height path parameter	0.6	-
b_{booth}	Width path parameter	1.6	-
–	Maximum tether length	80	m
–	Maximum tether length	200	m
T	Turbulence intensity	10	%

The instantaneous power produced by the kite system for both cases can is shown in Figure 4. The cycle-averaged power for the baseline case was 72.13 kW, while for the optimized case the power was 78.84 kW. This is a 9.3 percent improvement. The average flow speed at the kite's center of mass was 1.22 m/s for the baseline case and 1.24 m/s for the optimized case. This modest increase in local flow speed alone would only account for a 5 percent cycle-averaged power improvement for a constant elevation angle and spooling rate; however, by strategically adjusting the elevation angle and spooling profile, a more significant performance improvement can be realized.

The optimized spool-out profile and path center elevation angle profile can be seen in Figure 5. The discontinuities in the plots arise from the fact that the kite's operation is modal, with power generation (through spool-out operation) only occurring during a portion of the kite's operation. The turbulent flow velocity seen by the kite's center of mass is shown in Fig. 6 The kite speed versus time and tension versus time plot can be seen in Figures 7 and 8. the average spool speed for the baseline case was 0.4 m/s, which is faster than the spool speeds seen in Figure 5. Due to the slower spool speeds, the tensions and kite speeds are higher for the optimized case.

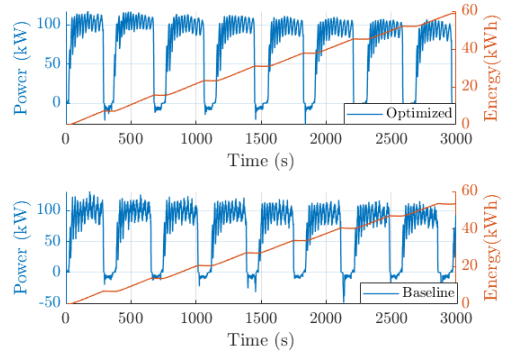

Fig. 4. Instantaneous power production for the kite system for both the baseline and optimized test cases.

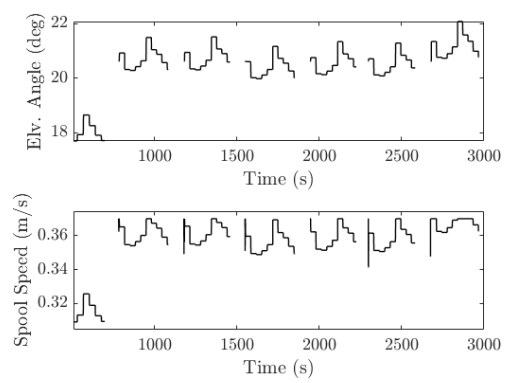

Fig. 5. The control inputs from spool-out phase optimization, which includes the path center elevation angle and spool-out rate command.

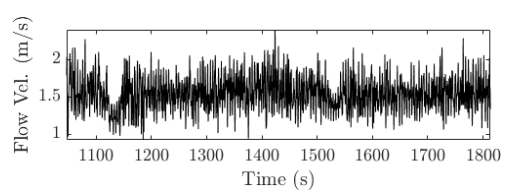

Fig. 6. The flow velocity magnitude at the kite's center of mass for the optimized case.

VI. Conclusion

This work presented and validated a transition controller and spool-out optimization algorithm for an energy-harvesting ocean kite. The transition controller allows the kite to smoothly and robustly execute a multi-cycle spooling strategy that consists of high-tension cross-current spool-out motion that is followed by low-tension radial spool-in motion. The optimization algorithm adjusts the spool-out speed profile and elevation angle profile at each cycle to

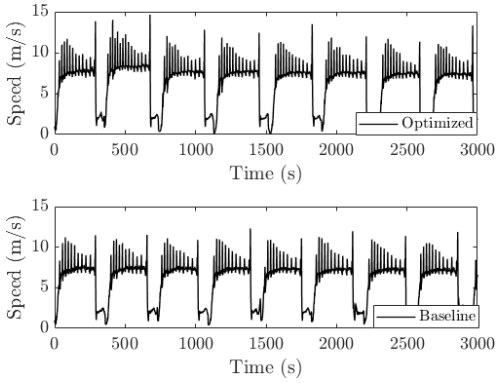

Fig. 7. Kite speed profile for the kite system for both the baseline and optimized test cases

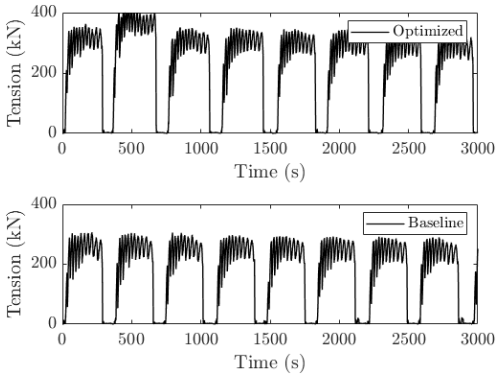

Fig. 8. Tether tension profile for the kite system for both the baseline and optimized test cases.

generate maximum cycle-averaged power output. Simulation results, which are based on a multi-body kite and tether model along with a spatiotemporally varying flow model, demonstrate robust flight performance and a 9.3 percent performance improvement as a result of the spooling speed and elevation angle profile optimization.

References

[1] K. A. Haas, H. M. Fritz, S. P. French, B. T. Smith, and V. Neary, "Assessment of energy production potential from tidal streams in the United States," 2011, Georgia Tech Research Corporation.

[2] K. A. Haas, H. M. Fritz, S. P. French, and V. Neary, "Assessment of energy production potential from ocean currents along the United States coastline," 2013, Georgia Tech Research Corporation.

[3] ARPA-E SHARKS. [Online]. Available: https://arpa-e.energy.gov/?q=arpa-e-programs/sharks

[4] A. LiVecchi, A. Copping, D. Jenne, A. Gorton, R. Preus, G. Gill, R. Robichaud, R. Green, S. Geerlofs, S. Gore, D. Hume, W. McShane, C. Schmaus, and H. Spence, "Powering the blue economy: Exploring opportunities for marine renewable energy in maritime markets," *U.S. Department of Energy*, 2019.

[5] X. Zeng and R. He, "Gulf Stream variability and a triggering mechanism of its meander in the South Atlantic Bight," *Journal of Geophysical Research - Oceans*, vol. 121, 2016.

[6] K. Archer and K. Caldeira, "Atlas of high altitude wind power," *Carnegie Institute for Science*, 2008.

[7] Windlift, "Windlift website," 2019. [Online]. Available: www.windlift.com

[8] Makani, "Makani website," 2019. [Online]. Available: makanipower.com

[9] Ampyx, "Ampyx power website," 2019. [Online]. Available: www.ampyxpower.com

[10] Altaeros Energies. [Online]. Available: http://www.altaeros.com/

[11] Minesto, "Minesto website," 2019. [Online]. Available: www.minesto.com

[12] D. J. Olinger and Y. Wang, "Hydrokinetic energy harvesting using tethered undersea kites," *Journal of Renewable and Sustainable Energy*, vol. 7, no. 4, p. 043114, 2015.

[13] A. Ghasemi, D. J. Olinger, and G. Tryggvason, "Computational simulation of the tethered undersea kites for power generation," in *ASME 2015 International Mechanical Engineering Congress and Exposition*. American Society of Mechanical Engineers, 2015, pp. V06BT07A043–V06BT07A043.

[14] H. Li, D. J. Olinger, and M. A. Demetriou, "Control of a tethered undersea kite energy system using a six degree of freedom model," in *2015 54th IEEE Conference on Decision and Control (CDC)*. IEEE, 2015, pp. 688–693.

[15] M. Loyd, "Crosswind kite power," *Journal of Energy*, vol. 4, no. 3, pp. 106–111, 1980.

[16] P. Williams, B. Lansdorp, and W. Ockesl, "Optimal crosswind towing and power generation with tethered kites," *Journal of guidance, control, and dynamics*, vol. 31, no. 1, pp. 81–93, 2008.

[17] B. Houska and M. Diehl, "Optimal control of towing kites," in *Proceedings of the 45th IEEE Conference on Decision and Control*. IEEE, 2006, pp. 2693–2697.

[18] L. T. Paiva and F. A. Fontes, "Optimal control of underwater kite power systems," in *2017 International conference in energy and sustainability in small developing economies (ES2DE)*. IEEE, 2017, pp. 1–6.

[19] M. Cobb, K. Barton, H. Fathy, and C. Vermillion, "An iterative learning approach for online flight path optimization for tethered energy systems undergoing cyclic spooling motion," in *2019 American Control Conference*, 2019, pp. 2164–2170.

[20] J. Daniels, J. Daniels, M. Cobb, A. Siddiqui, and C. Vermillion, "Optimal cyclic spooling control for kite-based energy systems," in *2020 International Federation on Automatic Control (IFAC) World Congress*, May 2020, accepted to IFAC Conference 2020.

[21] L. Fagiano, M. Milanese, and D. Piga, "Optimization of airborne wind energy generators," *International Journal of robust and nonlinear control*, vol. 22, no. 18, pp. 2055–2083, 2012.

[22] J. Reed, J. Daniels, A. Siddiqui, M. Cobb, and C. Vermillion, "Optimal exploration and charging for an autonomous underwater vehicle with energy-harvesting kite," in *2020 American Control Conference (ACC)*. IEEE, 2020, pp. 4134–4139.

[23] C. Vermillion, T. Grunnagle, R. Lim, and I. Kolmanovsky, "Model-based plant design and hierarchical control of a prototype lighter-than-air wind energy system, with experimental flight test results," *IEEE Transactions on Control Systems Technology*, vol. 22, pp. 531–542, 2014.

[24] T. I. Fossen, *Handbook of marine craft hydrodynamics and motion control*. John Wiley & Sons, 2011.

[25] M. Drela and H. Youngren. (2017) AVL. [Online]. Available: http://web.mit.edu/drela/Public/web/avl/

[26] J. Reed, M. Cobb, J. Daniels, A. Siddiqui, M. Muglia, and C. Vermillion, "Hierarchical control design and performance assessment of an ocean kite in a turbulent flow environment," in *2020 International Federation on Automatic Control (IFAC) World Congress*, May 2020, accepted to IFAC Conference 2020.

[27] Z. Yang and A. Copping, *Marine Renewable Energy: Resource Characterization and Physical Effects*. Springer, 2017.

[28] P. Pyakurel, J. H. VanZwieten, M. Dhanak, and N. I. Xiros, "Numerical modeling of turbulence and its effect on ocean current turbines," *International Journal of Marine Energy*, vol. 17, pp. 84–97, 2017.

[29] S. Rapp, R. Schmehl, E. Oland, S. Smidt, T. Haas, and J. Meyers, "A modular control architecture for airborne wind energy systems," in *AIAA Scitech 2019 Forum*, 2019, p. 1419.